

Feedback control of local hotspot temperature using resistive on-substrate nanoheater/thermometer

Amun Jarzembki, Sina Hamian, Jeonghoon Yun, Jacob Crossley, Inkyu Park, Mathieu Francoeur, and Keunhan Park

Citation: [Review of Scientific Instruments](#) **89**, 064902 (2018); doi: 10.1063/1.5020884

View online: <https://doi.org/10.1063/1.5020884>

View Table of Contents: <http://aip.scitation.org/toc/rsi/89/6>

Published by the [American Institute of Physics](#)



Feedback control of local hotspot temperature using resistive on-substrate nanoheater/thermometer

Amun Jarzembki,¹ Sina Hamian,² Jeonghoon Yun,³ Jacob Crossley,¹ Inkyu Park,³ Mathieu Francoeur,¹ and Keunhan Park^{1,a)}

¹Department of Mechanical Engineering, University of Utah, Salt Lake City, Utah 84112, USA

²CaSTL Center, Department of Chemistry, University of California, Irvine, California 92697, USA

³Department of Mechanical Engineering, Korea Advanced Institute of Science and Technology, Daejeon 305-701, South Korea

(Received 28 December 2017; accepted 24 May 2018; published online 13 June 2018)

This article reports the active control of a local hotspot temperature for accurate nanoscale thermal transport measurement. To this end, we have fabricated resistive on-substrate nanoheater/thermometer (NH/T) devices that have a sensing area of $\sim 350 \text{ nm} \times 300 \text{ nm}$. Feedback-controlled temporal heating and cooling experiments of the NH/T device confirm that the feedback integral gain plays a dominant role in device's response time for various setpoint temperatures. To further verify the integration of the feedback controller with the NH/T devices, a local tip-induced cooling experiment is performed by scanning a silicon tip over the hotspot area in an atomic force microscope platform. By carefully optimizing the feedback gain and the tip scan speed, we can control the hotspot temperature with the accuracy of $\sim \pm 1 \text{ K}$ for a broad range of setpoints from 325 K to 355 K. The obtained tip-substrate thermal conductance, including the effects of solid-solid conduction, water meniscus, air conduction, and near-field thermal radiation, is found to be a slightly increasing function of temperature in the range of 127 ± 25 to $179 \pm 16 \text{ nW/K}$. Our work demonstrates the reliable controllability of a local hotspot temperature, which will allow the further improvement of various nanoscale thermal metrologies including scanning thermal microscopy and nanoscale thermometry. *Published by AIP Publishing.* <https://doi.org/10.1063/1.5020884>

I. INTRODUCTION

Nanoscale thermometry is vital for the experimental characterization of sub-continuum thermal transport, such as nanoscale solid conduction,^{1–10} near-field thermal radiation,^{11–17} and heat transfer in atomic junctions.^{18–20} At such small scales, thermal transport greatly deviates from macroscale observations due to size effects like boundary scattering of phonons and electrons in heat conduction^{21,22} and photon tunneling in near-field thermal radiation.²³ Therefore, to understand the underlying physics of sub-continuum thermal transport, nanoscale thermometry should be implemented to quantify both the temperature gradient and heat transfer rate for geometric constrictions typically much smaller than $1 \mu\text{m}$. To date, nanoscale thermometry techniques have been developed within several platforms including near-field optical microscopy,^{24,25} resistive²⁶ or thermocouple^{3,6,11–13,27} scanning thermal microscopies, and on-substrate resistive^{1,2,7} or thermocouple^{28,29} thermometries: detailed reviews of these techniques can be found elsewhere.^{30,31} While advancements in nanothermometry have enabled groundbreaking experimental research in sub-continuum thermal transport, not many studies have implemented temperature feedback control of small-scale thermometry devices. In application based technologies, temperature feedback control of microelectromechanical systems has been used to improve measurement

stability and reduce thermal drift.³² To experimentally investigate thermal transport between a heated atomic force microscope (AFM) tip and on-substrate resistive nanothermometer, Park *et al.*¹ implemented temperature feedback control of the thermal cantilever to maintain an elevated heater temperature up to 750 K. For this case, the input current required to maintain the microheater temperature was used to compute the heat transfer rate through the tip. However, no work has combined temperature feedback control with nanothermometry to actively control a local hotspot temperature.

There are two major challenges when conducting experiments without local temperature feedback control: (1) undesirable variations in the heat transfer rate to the surrounding environment due to the change of the heater temperature and (2) uncontrolled temperature dependencies in the nanoscale thermal resistance of interest. These challenges often lead to measurement ambiguity because the temperature dependence of the nanoscale thermal system is not fully constrained. To address these challenges, we have combined resistive on-substrate nanoheater/thermometer (NH/T) devices with a closed-loop temperature feedback control scheme. The key advantage of using resistive thermometry is its simultaneous use as both a heater and thermometer. The design of our NH/T devices with feedback control enables the independent measurement of both temperature and power dissipation of the sensing area (or hotspot) at a sub-micron spatial resolution of $\sim 350 \text{ nm} \times 300 \text{ nm}$. Section II introduces the electrical setup used to operate the NH/T device and the design of the temperature feedback controller. Then, the performance of the

^{a)}Author to whom correspondence should be addressed: kpark@mech.utah.edu

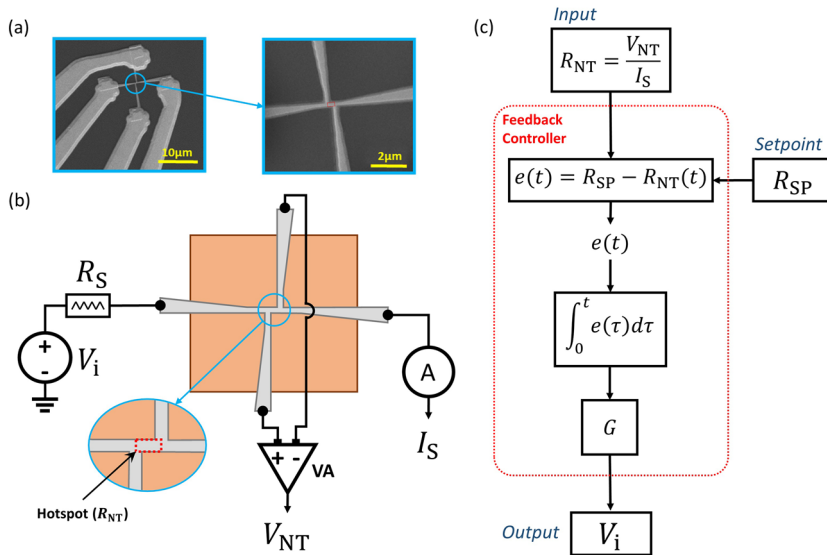


FIG. 1. (a) SEM images of a 4-probe resistive nanoheater/thermometer (NH/T) at low magnification (left) and high magnification (right). (b) Measurement principle of the NH/T, where V_i is the input circuit voltage, I_S is the current flow through the heater region measured using a current preamplifier, V_{NT} is the nanothermometer voltage measured with the differential voltage amplifier (VA), and R_S is a sense resistor of 0.5 k Ω . The local hotspot is denoted by the small region at the center of the device whose electrical resistance is R_{NT} . (c) Block diagram of the implemented feedback controller, which has R_{NT} as the measured process value, R_{SP} as the user-defined setpoint, and V_i as the output. G is controller's feedback gain that governs response time.

designed feedback controller is verified for different feedback gains and temperature setpoints. Section III presents a tip-induced cooling experiment in air using an AFM probe tip as a point heat sink. It is observed that when the AFM probe tip is in contact with the hotspot, the feedback controller increases the input power to compensate the heat loss to the tip. The effects of the sample scan speed and hotspot temperature on the performance of the feedback controller are studied. Finally, the temperature-dependent behaviors of the tip-induced local cooling and the effective tip-substrate thermal conductance are investigated, which demonstrates the effectiveness of implementing temperature feedback control for the measurement of nanoscale thermal transport.

II. INTEGRATION OF THE NH/T DEVICE WITH FEEDBACK CONTROL

The NH/T devices used for the present study are fabricated by combining e-beam lithography for nanopatterning and photolithography for micropatterning: more details of the device fabrication can be found in Ref. 2. Figure 1(a) shows scanning electron microscope (SEM) micrographs of a typical NH/T device, which is designed to operate with a 4-probe detection scheme. As illustrated in Fig. 1(b), an electric current (I_S) flows through the outer electrical leads to Joule heat a sub-micron platinum (Pt) pattern. The electrical resistance of the local hotspot (R_{NT}) can be measured by $R_{NT} = V_{NT}/I_S$, where V_{NT} is the voltage drop across the inner electrical leads. This configuration allows real-time monitoring of the local hotspot temperature (T_{NT}) at the center of the Pt wire, as denoted in the inset. The external circuit consists of a voltage source (V_i), an in-series sensing resistor ($R_s = 0.5$ k Ω), a current preamplifier (Femto, DLPCA-200), and a differential voltage amplifier (Texas Instruments, INA103). The input impedance of the voltage amplifier is 60 M Ω , which is 4 orders of magnitude larger than the circuit resistances and thus can prevent parasitic current flow through it. As shown in more details in Secs. I and II of the [supplementary material](#), the calibration data of three NH/T devices used for the present study (i.e., NH/T 1, NH/T 2, and

NH/T 3) exhibit a linear relationship between T_{NT} and R_{NT} . Moreover, the local hotspot can be Joule heated over 365 K under ambient conditions, further demonstrating the capability of the devices to act simultaneously as a heater and thermometer. The thermal resistance of the hotspot is measured to be $\sim 1 \times 10^6$ K/W, which is on the same order as other state-of-the-art nanothermometry techniques.^{13,19,33}

Figure 1(c) provides a block diagram of the feedback controller used to maintain R_{NT} , enabling constant temperature operation of NH/T's hotspot area. It is based on a proportional-integral (PI) controller that is predominantly governed by the integral component. Therefore, the use of the term *feedback gain* explicitly refers to controller's integral gain. The temperature control setup is conveniently integrated into the AFM controller (RHK Technology, R9) and has the same performance as the feedback controllers used during AFM operation. It has two inputs: the instantaneous value of $R_{NT}(t)$ and the user-defined resistance setpoint (R_{SP}).^{34–36} The instantaneous tracking error, $e(t)$, is computed based on the difference between R_{SP} and $R_{NT}(t)$, where the integration of $e(t)$ over the temporal variable τ from 0 to t provides the accumulation of past errors. The input voltage to the NH/T circuit (V_i) is updated by multiplying the feedback gain (G) with the temporal integration of the tracking error,³⁶

$$V_i(t) = G \int_0^t [R_{SP} - R_{NT}(\tau)] d\tau + V_i(0), \quad (1)$$

where $V_i(0)$ is the input voltage at $t = 0$ and G takes on a positive polarity to accommodate the direct variation of R_{NT} with changes in V_i . It should be noted that the unit of G is V/ Ω -s.

Figure 2 shows the temporal response of the NH/T in air during feedback control of hotspot's resistance, R_{NT} , upon a step-wise change of the resistance setpoint, ΔR_{SP} . The device used for this measurement (NH/T 1) has a room temperature resistance of 15 Ω and a temperature coefficient of resistance (TCR) of 6×10^{-4} K $^{-1}$. The hotspot size of NH/T 1 is measured to be 275 nm \times 250 nm \times 40 nm from the AFM topography. The temporal heating and cooling responses are shown in Figs. 2(a)

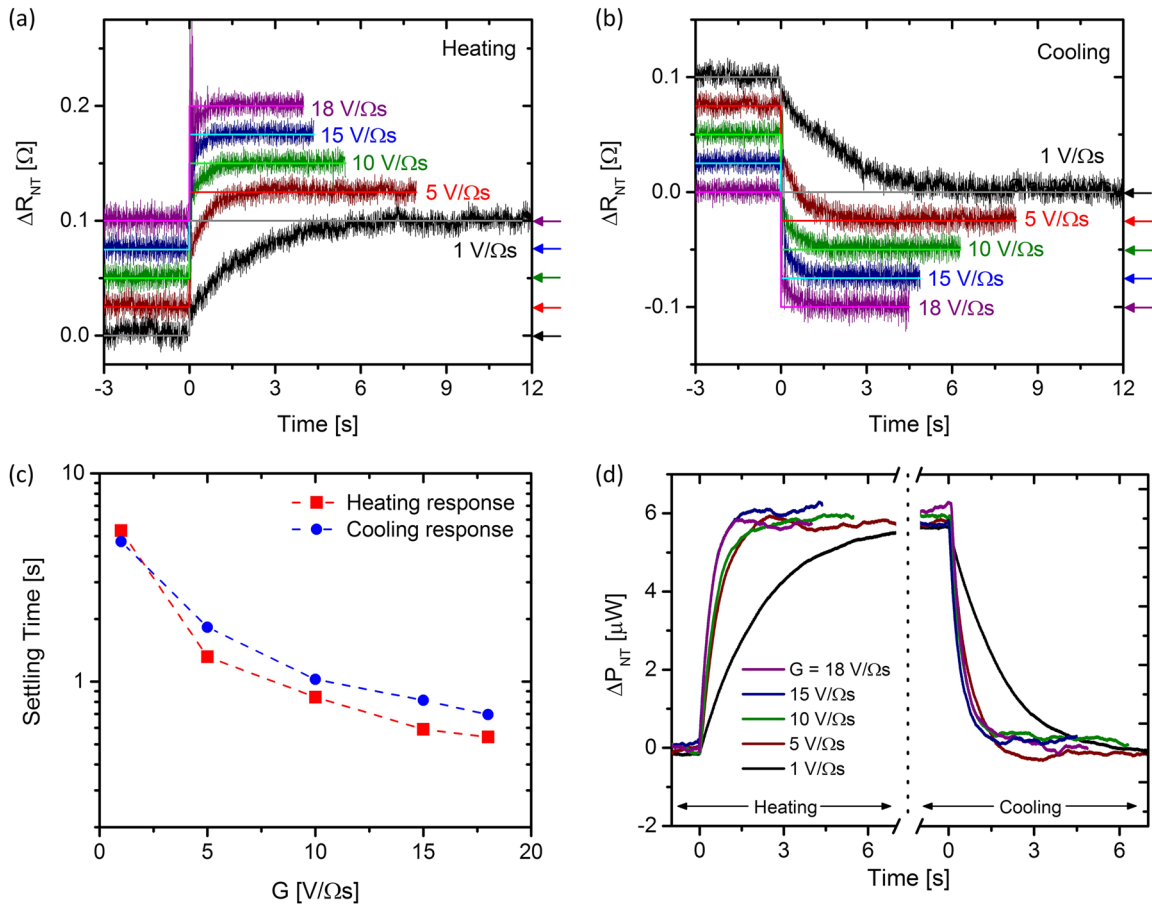


FIG. 2. (a) Measured temporal response of hotspot’s electrical resistance (R_{NT}) while increasing the resistance setpoint (solid lines) by $\Delta R_{SP} = 0.1 \Omega$ (i.e., $\Delta T_{NT} \approx 11 \text{ K}$) for different feedback gains. (b) The same as (a) but for decreasing the setpoint by $\Delta R_{SP} = -0.1 \Omega$. The curves in (a) and (b) have been offset by 0.025Ω illustrated by the colored arrows. (c) The settling time required to be within the noise threshold of the final setpoint, extracted from (a) and (b). (d) Change in power dissipation of the hotspot, ΔP_{NT} , during heating and cooling corresponding to the ΔR_{NT} responses in (a) and (b), respectively.

and 2(b), respectively, for different feedback gains (i.e., $G = 1, 5, 10, 15,$ and $18 \text{ V}/\Omega\text{-s}$). Solid lines in the figures show the resistance setpoint, $\Delta R_{SP} = 0.1 \Omega$, corresponding to $\Delta T_{NT} \approx 11 \text{ K}$. It should be noted that the curves are offset by 0.025Ω to clearly show the obtained results. For the heating case, the

feedback controller increases V_i to heat the device, subsequently raising R_{NT} to trace the setpoint, where the inverse is observed for the cooling case. The results clearly show that the feedback controller with a larger G allows a quick response to the stepwise setpoint change. However, an excessively large

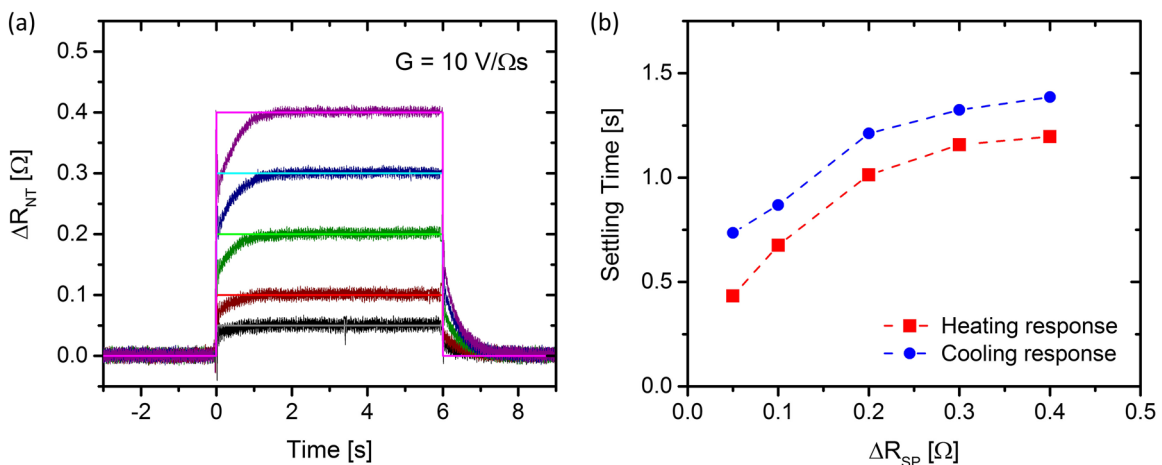


FIG. 3. (a) Measured temporal response of R_{NT} while increasing the resistance setpoint (solid lines) by ΔR_{SP} variations of $0.05, 0.1, 0.2, 0.3,$ and 0.4Ω (i.e., ΔT_{NT} variations of approximately $5.6, 11, 23, 34,$ and 45 K , respectively) for a constant gain of $G = 10 \text{ V}/\Omega\text{-s}$. (b) The settling time required to be within the noise threshold of the final setpoint extracted from (a). Larger resistance (or temperature) variations result in slower response in both heating and cooling.

G value may cause overshooting and often produces unstable output signals, as shown for $G = 18$ V/ Ω -s in Fig. 2(a). For NH/T 1, the resistance noise was found to be 6 m Ω leading to a temperature and power noise of 0.55 K and 114 nW, respectively: Details are provided in Sec. II of the [supplementary material](#). The settling time of the NH/T device is then defined as the time it takes for the hotspot response to reach within the resistance noise level around the setpoint. Figure 2(c) shows the settling time determined from Figs. 2(a) and 2(b), which asymptotically approaches ~ 600 ms as G increases. The associated power dissipated by the hotspot ($P_{\text{NT}} = I_s \times V_{\text{NT}}$) under feedback control is shown in Fig. 2(d) for both heating and cooling cases. The local hotspot dissipates nearly 6 μW while heating the NH/T by 0.1 Ω (i.e., ≈ 11 K).

Another study was performed using NH/T 1 on the temporal response of the device for ΔR_{SP} variations of 0.05, 0.1, 0.2, 0.3, and 0.4 Ω (or $\Delta T_{\text{NT}} \approx 5.6, 11, 23, 34,$ and 45 K, respectively), while the feedback gain is set to 10 V/ Ω -s. As shown in Fig. 3(a), a bigger step change of the setpoint gives rise to slower response of the hotspot temperature. Figure 3(b) confirms this trend by presenting the settling time as a function of ΔR_{SP} . The settling time is on the order of several hundred milliseconds for a small setpoint change, but it increases to 1.25 s at $\Delta R_{\text{SP}} = 0.4$ Ω . Heating is found to be slightly faster than cooling because cooling relies on ambient dissipation. This illustrates that temporal response of the hotspot is also

governed by the applied temperature gradient between the hotspot region and the substrate. The obtained results show that the 4-probe resistive NH/T devices can be successfully integrated with a PI feedback controller to maintain hotspot's resistance yielding constant temperature operation.

III. FEEDBACK CONTROL OF TIP-INDUCED HOTSPOT COOLING

To examine the feasibility of using a feedback-controlled NH/T device for nanoscale thermal transport measurement, a local cooling experiment is performed by scanning over the heated hotspot area with a silicon AFM probe (Bruker, FMV-A) in contact mode. Figure 4(a) illustrates the schematics of the experimental setup. The inset shows a typical SEM image of the tip used for the experiment, which has a pyramidal shape with nominal tip radius of ~ 10 nm. The AFM topography of the NH/T device is shown in Fig. 4(b). While typical values of R_{NT} range from 10 to 30 Ω depending on the batch fabrication conditions, this particular NH/T device (NH/T 2) has a room temperature resistance of 21.09 ± 0.01 Ω , a volumetric sensing probe size of $350 \text{ nm} \times 300 \text{ nm} \times 40 \text{ nm}$, and a TCR of 8×10^{-4} K^{-1} . Figures 4(c) and 4(d) present temperature and power dissipation images ($4 \mu\text{m} \times 4 \mu\text{m}$ with 512×128 pixels) taken by scanning the AFM tip from left to right (forward) around the hotspot area, while Figs. 4(e) and 4(f) provide the same images

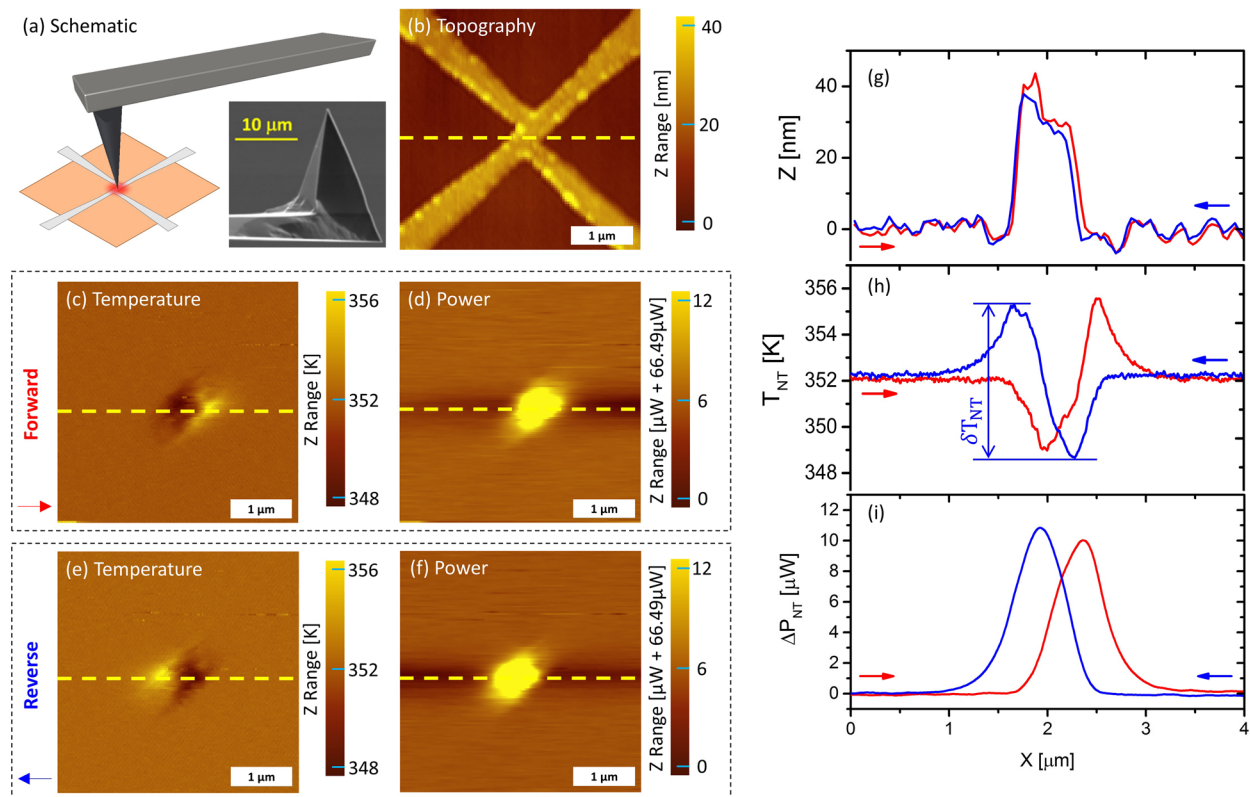


FIG. 4. (a) Schematic of the tip-induced cooling experiment where a cold AFM tip (a typical SEM image shown in the inset) at 300 K is brought into contact with the hotspot area at 352 K. (b) Topography ($4 \mu\text{m} \times 4 \mu\text{m}$) of the NH/T device with room temperature resistance of 21.09 ± 0.01 Ω . (c) Temperature and (d) power dissipation maps during contact-mode scanning in the forward (red) direction. (e) and (f) The same as (c) and (d) for contact-mode scanning in the reverse (blue) direction. Arrows in the lower left corners illustrate the direction of tip motion. Scan lines extracted from the yellow dashed lines in (b)–(f) showing (g) forward and reverse topography; (h) forward and reverse temperature, T_{NT} ; and (i) forward and reverse tip-induced power dissipation, ΔP_{NT} .

for the right-to-left (reverse) scan direction. The images were acquired with a scan speed of $1 \mu\text{m/s}$ and a contact force of $\sim 5 \text{ nN}$ to ensure AFM stability and probe longevity, while the hotspot temperature is feedback-controlled at 352.1 K (or $R_{\text{NT}} = 21.9 \Omega$). The feedback gain was set to $5 \text{ V}/\Omega\text{-s}$, which was optimized for the NH/T 2 device to ensure a settling time shorter than 1 s without overshooting in the hotspot temperature response. The temperature scanning image under feedback control shows scan direction dependence where the darker region corresponds to the leading edge of the NH/T followed by a brighter region at the trailing edge. The dark region is due to momentary cooling as the tip scans over the NH/T, which is recovered to the setpoint by increasing the power input to the device as shown in Figs. 4(d) and 4(f). However, the feedback control is not fast enough to fully respond to the tip-scanning speed ($1 \mu\text{m/s}$), resulting in overheating of the hotspot as represented by the bright region in the temperature image. Meanwhile, the power input is gradually reduced to stabilize the hotspot temperature. Figure 4 also shows the line-scan profiles of the NH/T's (g) topography, (h) temperature response, and (i) power dissipation, all extracted from the yellow dashed lines in Figs. 4(b)–4(f). The peak-to-peak temperature fluctuation (δT_{NT}) around its setpoint is clearly observed in Fig. 4(h) and is found to be about 6 K . In addition, the scan direction dependence of the tip power dissipation (ΔP_{NT}) has a 438 nm separation between the two peaks of $\sim 10 \mu\text{W}$. The two peaks also have different magnitudes, which is attributed to the non-uniform NH/T topography shown in Fig. 4(g). The observed δT_{NT} and the shift of the peak in ΔP_{NT} are due to a mismatch between the feedback gain and tip-scanning speed, suggesting that they should be optimized for more reliable tip-induced cooling experiments under feedback control.

Figure 5 shows the effect of tip scan speed on δT_{NT} and ΔP_{NT} when T_{NT} is feedback-controlled at 342 K . For clarity, ΔP_{NT} is the difference in power dissipation when the tip is on and off the device sensing area, which may represent the transient tip-induced local cooling rate. The NH/T device for these measurements (NH/T 3) has a room temperature resistance of $12.24 \pm 0.01 \Omega$, sensing volume size of $275 \text{ nm} \times 350 \text{ nm} \times 50 \text{ nm}$, and TCR of $5 \times 10^{-4} \text{ K}^{-1}$, requiring a feedback gain of $14 \text{ V}/\Omega\text{-s}$ for reliable operation at scan speeds from 0.3 to $6 \mu\text{m/s}$. At high scan speeds, the temperature is not well maintained by the feedback controller, leading to a large δT_{NT} . For scan speeds $> 2 \mu\text{m/s}$, the increase of δT_{NT} leads to a plateau due to a scan speed that is faster than the thermal response of the NH/T device. Our previous work revealed that the NH/T devices are not sufficiently cooled by the tip for scan speeds higher than $2 \mu\text{m/s}$.² As the scan speed decreases, δT_{NT} decreases significantly because more time is allotted for the controller to stabilize its output. This is clearly seen in the inset which compares representative forward scan lines (tip motion left to right) for the $0.3 \mu\text{m/s}$ (blue) and $6 \mu\text{m/s}$ (red) scan speeds. The effect of scan speed is also observed in the tip-induced power dissipation, where a fast scan speed results in the decrease of ΔP_{NT} due to the slow response of the feedback controller. For example, as the tip motion increases from 0.3 to $6 \mu\text{m/s}$, ΔP_{NT} decreases by more than half. The slow feedback control at $6 \mu\text{m/s}$ can also be confirmed by the lag of the ΔP_{NT}

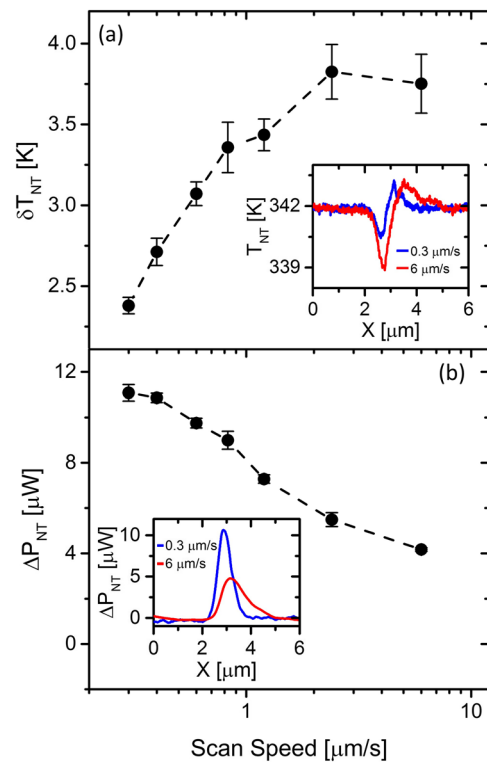


FIG. 5. Scan speed dependence of (a) the peak-to-peak temperature fluctuation (δT_{NT}) and (b) the tip-induced power dissipation (ΔP_{NT}) for the hotspot temperature at 342 K and feedback gain of $14 \text{ V}/\Omega\text{-s}$. For faster scan speeds, the feedback controller needs more time to stabilize the hotspot temperature during operation. Insets show scan lines for the fastest (red) and slowest (blue) scan speed data points (tip motion left to right).

peak as shown in the inset. As the scan speed decreases, ΔP_{NT} is saturated to $\sim 11 \mu\text{W}$, which is attributed to the steady heat transfer to the tip. The obtained result is in good qualitative agreement with the finite element analysis results as discussed in more details in Sec. III of the [supplementary material](#). From Fig. 5, the local hotspot's heating/cooling rate plays a dominant role on feedback performance and must be accounted for in addition to the effect of feedback gain shown in Fig. 2.

Figure 6(a) presents ΔP_{NT} for a broad range of T_{NT} ($322.8 \text{ K} < T_{\text{NT}} < 354.9 \text{ K}$) during contact-mode scanning in air. The measurements were taken using a scan speed of $0.6 \mu\text{m/s}$ and feedback gain of $14 \text{ V}/\Omega \text{ s}$ to ensure proper response of the feedback controller to the tip-induced cooling for NH/T 3. By increasing the hotspot temperature, there is a larger potential for heat transfer between the hot substrate and cool tip leading to a well correlated trend between tip-induced thermal transport and substrate temperature. Each of the 112 measurements were extracted from individual ΔP_{NT} line traces over the hotspot area (similarly observed in Fig. 4), where uncertainty induced by AFM scanning is included. To better interpret the data, a statistical analysis is performed by generating the best-fit linear regression (red dashed line, R^2 correlation of 0.84) and the $\pm 1\sigma$ uncertainty (red shaded region) of the data. The uncertainty in ΔP_{NT} is shown to increase with T_{NT} . To understand this better, Fig. 6(b) shows δT_{NT} for the 112 different hotspot temperatures between $322.8 \pm 0.6 \text{ K}$ and 354.9

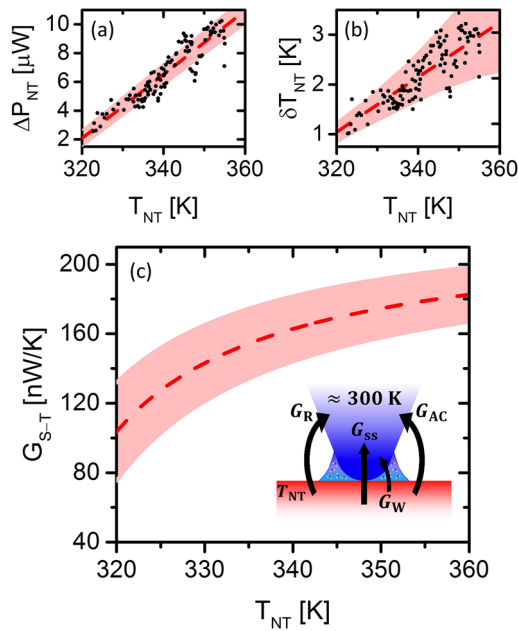


FIG. 6. (a) Variation of the tip-induced power dissipation (ΔP_{NT}) as a function of the hotspot temperature (T_{NT}). The dashed line shows linear regression with R^2 correlation of 0.84, while the shaded region shows the $\pm 1\sigma$ range of the experimental data. (b) Effect of T_{NT} on δT_{NT} . The statistical data analysis in (a) is used to present (c) the temperature dependence of the effective tip-substrate thermal conductance (G_{S-T}), which includes the effects of solid-solid conduction (G_{SS}), water meniscus (G_W), air conduction (G_{AC}), and near-field thermal radiation (G_R) as shown in the inset. All scanning measurements were conducted with a constant scan speed of $0.6\ \mu\text{m/s}$ and feedback gain of $14\ \text{V}/\Omega\text{-s}$.

$\pm 1.5\ \text{K}$. Here higher values of T_{NT} cause δT_{NT} to increase up to nearly $3\ \text{K}$ at $355\ \text{K}$. However, for $T_{NT} = 325\ \text{K}$, δT_{NT} approaches the noise threshold of the NH/T device (i.e., $\pm 0.5\ \text{K}$).

The effective thermal conductance between the substrate and tip is defined as $G_{S-T} = \Delta P_{NT}/(T_{NT} - T_{\text{tip}})$, where T_{tip} is the tip apex temperature. Since T_{tip} is difficult to measure without the use of a functionalized thermocouple probe,^{10,12,13,16} we assume that the tip thermal resistance is much smaller than the thermal resistance of the point contact, which leads to $G_{S-T} \approx \Delta P_{NT}/(T_{NT} - T_{\infty})$ with T_{∞} being room temperature. Figure 6(c) shows the resulting trend and $\pm 1\sigma$ uncertainty of G_{S-T} as a function T_{NT} . It should be noted that our measurement of G_{S-T} includes the effects of solid-solid conduction (G_{SS}), water meniscus (G_W), air conduction (G_{AC}), and near-field thermal radiation (G_R) such that $G_{S-T} = G_{SS} + G_W + G_{AC} + G_R$ as shown in the inset. G_{S-T} shows a weak temperature dependence changing from $127 \pm 25\ \text{nW/K}$ to $179 \pm 16\ \text{nW/K}$, while the hotspot temperature increases from $325\ \text{K}$ to $355\ \text{K}$. We believe that the increase of G_{S-T} at higher temperature is mainly due to the dominant contribution of air conduction. Previous experiments have reported results of tip-substrate thermal conductance in air¹⁻⁶ and vacuum⁷⁻¹⁰ environments. G_{SS} has been measured in the range from $1\ \text{nW/K}$ ⁸ to $\sim 100\ \text{nW/K}$ ⁹ depending on experimental geometry and selected materials, yet the majority of studies find $\sim 10\ \text{nW/K}$.^{1-3,10} However, G_{AC} can be as much as one order of magnitude larger than G_{SS} , dominantly contributing to the

effective tip-substrate thermal conductance of $\sim 100\ \text{nW/K}$.¹⁻³ While the obtained measurement is in good agreement with the aforementioned previous studies, it should be noted that the electrical leads outside the hotspot are heated as well during the feedback control operation and transfer more heat to the tip in addition to the power dissipation change at the hotspot. The heat transfer rate to the tip is then written as $Q_{\text{tip}} = \Delta P_{NT} + Q_{\text{lead}}$, where Q_{lead} is the additional heat transfer from the heater leads. Section III of the [supplementary material](#) discusses the details of the finite element analysis used to estimate the systematic uncertainty in the measurement of Q_{tip} due to the presence of Q_{lead} . Based on the computation results, we believe that $\sim 10\%$ of Q_{tip} may come from the outside heater leads. Therefore, a comprehensive measurement scheme and analytical model should be developed to experimentally determine the effect of Q_{lead} , which will be conducted in the near future.

IV. CONCLUSIONS

In this article, we have implemented temperature feedback control with resistive on-substrate nanoheater/thermometer (NH/T) devices enabling constant temperature operation of a submicron-sized local hotspot for various operational conditions. The response time of the feedback controller was found to be highly sensitive to the feedback gain, applied temperature setpoint, and electrical characterization of the device. In addition, a local cooling experiment with an AFM tip in contact mode demonstrates that the feedback controller is able to quickly adjust the local hotspot's temperature to a setpoint with $\sim \pm 1\ \text{K}$ fluctuations. Monitoring the power dissipation of the hotspot during tip scanning allows the examination of the tip-substrate heat transfer and associated thermal conductance. By performing measurements in ambient environment, the effective tip-substrate thermal conductance is measured to be $127 \pm 25\ \text{nW/K}$ at $325\ \text{K}$. The thermal conductance slightly increases to $179 \pm 16\ \text{nW/K}$ as the temperature increases to $355\ \text{K}$ mainly due to the effect of air conduction. Although a systematic uncertainty due to the presence of the outside leads should be further addressed, we believe that the developed instrumentation will provide a reliable experimental approach to nanoscale thermal transport measurements by actively controlling a local hotspot temperature.

SUPPLEMENTARY MATERIAL

See [supplementary material](#) for (1) calibration of NH/T devices; (2) DC noise analysis of NH/T devices; and (3) finite element analysis of NH/T devices under feedback control.

ACKNOWLEDGMENTS

This work was supported by the National Science Foundation (CBET-1605584) and the Nano Material Technology Development Program (2015M3A7B7045518) through the National Research Foundation of Korea (NRF). A.J. acknowledges financial supports from the University of Utah's Sid Green Fellowship and the National Science Foundation Graduate Research Fellowship (No. 2016213209). J.C.

acknowledges the support from the Undergraduate Research Opportunity Program (UROP) at the University of Utah.

- ¹K. Park, G. L. W. Cross, Z. M. Zhang, and W. P. King, *J. Heat Transfer* **130**, 102401 (2008).
- ²S. Hamian, J. Yun, I. Park, and K. Park, *Appl. Phys. Lett.* **109**, 253114 (2016).
- ³L. Shi and A. Majumdar, *J. Heat Transfer* **124**, 329 (2002).
- ⁴J. Lee, A. Liao, E. Pop, and W. P. King, *Nano Lett.* **9**, 1356 (2009).
- ⁵S. Sadat, A. Tan, Y. Chua, and P. Reddy, *Nano Lett.* **10**, 2613 (2010).
- ⁶P. C. Fletcher, B. Lee, and W. P. King, *Nanotechnology* **23**, 035401 (2012).
- ⁷F. Menges, H. Riel, A. Stemmer, and B. Gotsmann, *Nano Lett.* **12**, 596 (2012).
- ⁸F. Menges, P. Mensch, H. Schmid, H. Riel, A. Stemmer, and B. Gotsmann, *Nat. Commun.* **7**, 10874 (2016).
- ⁹M. Thompson Pettes, L. Shi, M. T. Pettes, and L. Shi, *J. Heat Transfer* **136**, 032401 (2013).
- ¹⁰K. Kim, W. Jeong, W. Lee, S. Sadat, D. Thompson, E. Meyhofer, and P. Reddy, *Appl. Phys. Lett.* **105**, 203107 (2014).
- ¹¹W. Muller-Hirsch, A. Kraft, M. T. Hirsch, J. Parisi, and A. Kittel, *J. Vac. Sci. Technol., A* **17**, 1205 (1999).
- ¹²A. Kittel, W. Muller-Hirsch, J. Parisi, S. A. Biehs, D. Reddig, and M. Holthaus, *Phys. Rev. Lett.* **95**, 224301 (2005).
- ¹³K. Kim, B. Song, V. Fernández-Hurtado, W. Lee, W. Jeong, L. Cui, D. Thompson, J. Feist, M. T. H. Reid, F. J. García-Vidal, J. C. Cuevas, E. Meyhofer, and P. Reddy, *Nature* **528**, 387 (2015).
- ¹⁴B. Guha, C. Otey, C. B. Poitras, S. Fan, and M. Lipson, *Nano Lett.* **12**, 4546 (2012).
- ¹⁵R. St-Gelais, B. Guha, L. Zhu, S. Fan, and M. Lipson, *Nano Lett.* **14**, 6971 (2014).
- ¹⁶K. Kloppstech, N. Köne, S.-A. Biehs, A. W. Rodriguez, L. Worbes, D. Hellmann, and A. Kittel, *Nat. Commun.* **8**, 14475 (2017).
- ¹⁷L. Cui, W. Jeong, V. Fernández-Hurtado, J. Feist, F. J. García-Vidal, J. C. Cuevas, E. Meyhofer, and P. Reddy, *Nat. Commun.* **8**, 14479 (2017).
- ¹⁸N. Mosso, U. Drechsler, F. Menges, P. Nirmalraj, S. Karg, H. Riel, and B. Gotsmann, *Nat. Nanotechnol.* **12**, 430 (2017).
- ¹⁹L. Cui, W. Jeong, S. Hur, M. Matt, J. C. Klöckner, F. Pauly, P. Nielaba, J. C. Cuevas, E. Meyhofer, and P. Reddy, *Science* **355**, 1192 (2017).
- ²⁰W. Lee, K. Kim, W. Jeong, L. A. Zotti, F. Pauly, J. C. Cuevas, and P. Reddy, *Nature* **498**, 209 (2013).
- ²¹T. Yamada, S. Hamian, B. Sundén, K. Park, and M. Faghri, *Int. J. Heat Mass Transfer* **61**, 287 (2013).
- ²²S. Hamian, T. Yamada, M. Faghri, and K. Park, *Int. J. Heat Mass Transfer* **80**, 781 (2015).
- ²³A. Jarzembski and K. Park, *J. Quant. Spectrosc. Radiat. Transfer* **191**, 67 (2017).
- ²⁴K. E. Goodson and M. Ashegh, *Microscale Thermophys. Eng.* **1**, 225 (1997).
- ²⁵Y. Yue, X. Chen, and X. Wang, *ACS Nano* **5**, 4466 (2011).
- ²⁶L. Bozec, A. Hammiche, M. Tobin, J. Chalmers, N. Everall, and H. Pollock, *Meas. Sci. Technol.* **13**, 1217 (2002).
- ²⁷C. C. Williams and H. K. Wickramasinghe, *Appl. Phys. Lett.* **49**, 1587 (1986).
- ²⁸D. Chu, D. Bilir, R. Pease, and K. Goodson, *J. Vac. Sci. Technol., B: Microelectron. Nanometer Struct.* **20**, 3044 (2002).
- ²⁹H. Liu, W. Sun, and S. Xu, *Adv. Mater.* **24**, 3275 (2012).
- ³⁰Y. Yue and X. Wang, *Nano Rev.* **3**, 11586 (2012).
- ³¹J. Lee and N. A. Kotov, *Nano Today* **2**, 48 (2007).
- ³²J. W. Gong, Q. F. Chen, M. R. Lian, N. C. Liu, and C. Daoust, *IEEE Sens. J.* **6**, 139 (2006).
- ³³K. Kim, W. Jeong, W. Lee, and P. Reddy, *ACS Nano* **6**, 4248 (2012).
- ³⁴K. Astrom and T. Hagglund, *PID Controllers: Theory, Design and Tuning* (Instrument Society of America, Research Triangle Park, NC, 1995).
- ³⁵J. Doyle, B. Francis, and A. Tannenbaum, *Feedback Control: Theory and Design* (Macmillan Publishing Co., 1990).
- ³⁶O. Beker, C. Hollot, and Y. Chait, *IEEE Trans. Autom. Control* **46**, 1797 (2001).